Network Model Investigation of Interfacial Area, Capillary Pressure and Saturation Relationships in Granular Porous Media

V. Joekar-Niasar,[1] M. Prodanović[2] D. Wildenschild,[3] and S. M.

Hassanizadeh,[1]

V. Joekar-Niasar, Department of Earth Sciences, Utrecht University, PO Box 80021, Utrecht,

3508 TA, The Netherlands. (joekar@geo.uu.nl)

[1]Department of Earth Sciences, Utrecht

University, PO Box 80021, Utrecht, 3508

TA, the Netherlands.

[2]CPGE, University of Texas at Austin, 1

University Station, C0304 Austin, TX

78712, USA

[3]School of Chemical, Biological and

Environmental Engineering, Oregon State

University, 103 Gleeson Hall Corvallis, OR

97331-2702, USA.

Abstract.   We have developed a new approach for generating pore throat cross sections of various shapes based on distributions of shape factors and radii of inscribed circles. These distributions are obtained from analysis of grains packing. General formulas for calculating geometrical properties and entry capillary pressure for given shape factor and inscribed circle radius are developed. These relationships are employed in a pore network, which has a number of special features. In particular, it is highly flexible in terms of location of pore bodies, variable coordination number, as well as variable cross-sectional shapes. The pore-network model is employed for simulating the equilibrium distribution of two fluids in a granular porous medium, under both drainage and imbibition conditions.

The pore-network model is verified by comparing simulation results with experimental data of quasi-static drainage and imbibition experiments in a glass-bead medium. The pore-level topology and geometrical description of pore bodies and pore throats, essential for building the network, are rigorously extracted from experimental data using image analysis (*3DMA-Rock* software). Calculated capillary pressure-saturation (P^c-S^w) and specific interfacial area-saturation (a^{nw}-S^w) curves show very good agreement with measured ones, for both drainage and imbibition. We show that the shape factor can significantly influence the form of macroscopic P^c-S^w and a^{nw}-S^w curves, if the length and volumes associated to the pore throats is considerable. Furthermore, using continuous generation of shape factor distribution, the model can be validated against the grain size distribution. After

validating the model against experiments, in addition to primary and main curves, we simulate many scanning curves to generate P^c-S^w-a^{nw} surfaces for drainage and imbibition, separately. Results show that these two surfaces lie very close to each other, and the average normalized difference is small, in the range of simulations uncertainty. Our results illustrate that P^c-S^w-a^{nw} surfaces show very little hysteresis and, therefore, specific interfacial area can be considered as an essential variable for reducing or eliminating the hysteresis observed in P^c-S^w curves.

1. Introduction

1.1. Pore-network Modeling

Among other sources, pore-scale information is very much needed for gaining insight in, and for fundamental understanding of, the physics of flow and transport in porous media. Thus, in recent years, various imaging techniques, such as X-ray computed microtomography [for recent overview see *Wildenschild et al.*, 2002; *Kaestner et al.*, 2008] and magnetic resonance imaging (MRI) have been employed to obtain detailed pore-scale information from many porous media. Combined with pore-scale modeling methods, such detailed information can be used to understand the interplay of various flow mechanisms and produce data for investigating macroscale theories. Depending on the pore-scale modeling technique, pore space geometry can be either used directly or as a simplified network of pores. Direct simulation techniques, such as Lattice-Boltzmann method [*Shan and Chen*, 1994; *Ahrenholz et al.*, 2008; *Schaap et al.*, 2007; *Porter et al.*, 2009], are computationally demanding. Thus, often pore-network models are used where the pore space is idealized as a network of "pore bodies" and "pore throats".

Pore-network models - pioneered by *Fatt* [1956] - have been extensively used to study a variety of flow and transport phenomena in porous media. They can be divided into quasi-static and dynamic ones. Quasi-static pore-network models simulate only equilibrium states of drainage and imbibition processes without solving the pressure field [see e.g. *Fatt*, 1956]. For a review of the literature, see *Celia et al.* [1995] and *Blunt* [2001]. But, dynamic pore-network models simulate the transient behavior of (multiphase) flow [see e.g.

Koplik and Lasseter, 1985; *Dias and Payatakes*, 1986; *Dahle and Celia*, 1999; *Nordhaug et al.*, 2003].

The main challenge in development of the structure of a pore network is to preserve essential features of the void space (relevant to multiphase flow). While representing the void space as a network of simplified geometries, it should be tractable for computations. Major characteristics of a pore network are its topology (i.e. positioning of pore bodies, and the number and orientation of links) and geometry of elements.

Regarding the topology, if pore bodies are centered at nodes of a regular lattice, the network is referred to as a "structured" network. The number of pore throats connected to a pore body is called "coordination number". Many pore-network models have a coordination number of six, with pore throats oriented along the three principal directions of the lattice. We refer to these as regular networks. But, there are some network models with variable coordination number and with pore throats oriented in many directions [see e.g. *Mogensen and Stenby*, 1998; *Piri and Blunt*, 2005; *Joekar-Niasar et al.*, 2009; *Raoof and Hassanizadeh*, 2009; *Ryazanov et al.*, 2009].

Geometry of the network is represented by shape and size of pore bodies and pore throats. Commonly, all pore bodies in a pore-network model are assigned the same shape, such as sphere [e.g. *Reeves and Celia*, 1996; *Bakke and Øren*, 1997; *Øren and Bakke*, 2002] or cube [e.g. *Mogensen and Stenby*, 1998; *Patzek*, 2001]. In yet some other models, no pore bodies are defined at all; i.e. no geometry is assigned to the connection points of pore throats. Instead, a variable cross section is assigned to each pore throat [see e.g. *Dias and Payatakes*, 1986]. However, an accurate representation of the exact geometry of large voids among grains in a real porous medium is not straight forward. Since pore

bodies are the controlling elements during imbibition, any inaccuracy in representation of pore bodies increases the difficulty of simulation of the imbibition process.

Similarly, different choices are made for the shape of pore throats. In many models, all pore throats are assigned the same cross-sectional shape [e.g. *Reeves and Celia*, 1996]. But pore networks where different cross-sectional shapes are assigned to various pore throats have been also developed. We refer to them as "mixed cross-sectional" pore networks [*Bakke and Øren*, 1997; *Patzek*, 2001; *Øren and Bakke*, 2002].

The cross-sectional shape of a pore throat is commonly parametrized by means of a shape factor. In two dimensions, the shape factor is defined as the ratio of cross-sectional area (A) to the square of the perimeter (P); $G = A/P^2$. The influence of shape factor on the entry capillary pressure, conductance, residual saturation, and interfacial area of a pore with triangular cross section was first studied by *Mason and Morrow* [1991]. Since then, shape factor has been used for specification of pore throats shapes especially in quasi-static pore-network models.

Bakke and Øren [1997] developed a pore-network model with mixed cross sections for actual sandstones. However, the range of shape factor that was recovered in their model was very limited (to 0.0481, which corresponds to an equilateral triangle). In a model by *Man and Jing* [2000], pore throats were assigned star-shape cross section with four vertices. However, the authors chose pore throat cross sections in an arbitrary fashion and did not compare their P^c-S^w curves with experiments. *Patzek* [2001] developed a network with cubic pore bodies and four different polygonal cross sections for pore throats. He simulated relative permeability-saturation (k_r-S^w) and capillary pressure-saturation (P^c-S^w) relationships for *Bentheimer* sandstone. The author did not specify

how the choice of specific cross-sectional shapes for pore throats and pore bodies was related to the sandstone geometrical properties. *Piri and Blunt* [2005] developed a pore-network model for two- and three-phase flow for a mixed-wet porous medium. They chose circular, square, and triangular shapes for pore throat cross sections, and simulated relative permeability curves for *Berea* sandstone. *Sholokhova et al.* [2009] developed a model with three different cross sections (triangle, rectangle and ellipse) to study single-phase absolute permeability. They compared their results with the experimental data for *Fontainebleau* sandstone. *Ryazanov et al.* [2009] developed an unstructured irregular network with star-shape pore throats without including pore bodies. The structure were derived from image analysis of *Berea* sandstone.

In all above-mentioned pore-network models the full range of shape factor distribution was not continuously generated. Since, for $G > 0.0481$ triangular cross sections cannot be used, regular polygons are applied. Consequently, the resulting network has a stepped shape factor distribution instead of a continuous one. In fact, for a given shape factor, many different (combinations of) cross-sectional shapes are possible. Therefore, one should investigate the effect of number of vertices of a pore throat cross section on the macroscale porous media properties.

1.2. Objectives

The focus of this work is two-fold.

a. We develop a well-defined procedure for the selection of the cross-sectional shape of pore elements based on image analysis data. Contrary to the previous pore networks, in this work, the choice of pore cross sections is linked either to the local shape factor or to the overall shape factor distribution. This allows us to recover the full shape factor

distribution continuously and avoid an arbitrary selection of polygonal cross sections. Furthermore, this approach gives us information about the gains size distribution, which can be checked against the actual grain size distribution.

We carefully select a mix of pore throat cross sections - irregular or regular hyperbolic polygons. This allows us to match pore-space topological and geometrical data obtained from micro-tomographic imaging for any given value of shape factor. We develop formulas for the entry capillary pressure of various shapes, which can be solved numerically. Pore bodies are represented by prolate spheroids. In this work, we have employed *3DMA-Rock* software [*Lindquist*, 2009] for image analysis.

b. Pore-network models have been mainly used to study standard concepts such as relative permeability and capillary pressure-saturation relationships. Here, we also study the role of fluid-fluid interfacial areas in elucidating and parameterizing capillary effects in a two-phase flow. In particular, we investigate the conjecture by *Hassanizadeh and Gray* [1990, 1993] that specific interfacial area, a^{nw} (defined as the amount of fluid-fluid interfacial area per unit volume of the porous medium) is a major state variable in two-phase flow and the main variable for proper modeling of capillary hysteresis.

This conjecture has been investigated earlier by *Reeves and Celia* [1996]; *Held and Celia* [2001]; *Joekar-Niasar et al.* [2008, 2009] using pore-network models. *Reeves and Celia* [1996]; *Held and Celia* [2001], and *Joekar-Niasar et al.* [2008] used regular structured pore networks with circular cross sections. *Reeves and Celia* [1996] and *Joekar-Niasar et al.* [2008] concluded that hysteresis can be significantly reduced by including a^{nw} to generate one surface defined $F(P^c, S^w, a^{nw}) = 0$. *Joekar-Niasar et al.* [2008] showed that with increase of aspect ratio (ratio of pore body radius to pore throat radius), effect of

a^{nw} in reducing the hysteresis decreases. However, their results were not compared with experiments. All these models lack some major structural features such as angularity of the cross sections and irregularity of the network. Thus, it is not clear whether the conclusions would hold in a real porous media with an unstructured irregular and angular pore network.

The only published comparison between pore-network results and experimental data in this regard is the work by *Joekar-Niasar et al.* [2009] who simulated drainage and imbibition experiments, performed in a two-dimensional micromodel. They generated imbibition and drainage P^c-S^w-a^{nw} surfaces and found that including a^{nw} reduced hysteresis. Since the micro-model was two-dimensional and had high porosity, the experiments had very uncommon features as follow. The saturation of the wetting phase changed between 0.68 and 1.0, so the range of saturation in P^c-S^w-a^{nw} surface was too limited. Due to the high porosity and small aspect ratio, the nonwetting phase did not trap at all during imbibition (no snap-off). This is very uncommon in practice. Furthermore, due to two-dimensionality of the model, the hysteresis in P^c-S^w curves was not significant (only about 20%) and the flow path was restricted to a three-dimensional medium.

In this work, we have developed a three-dimensional irregular unstructured pore-network model and validated it against experimental data. Data were obtained from air-water drainage and imbibition experiments in a glass-bead column and reported in *Culligan et al.* [2004]. We compare our results against measured capillary pressure-saturation (P^c-S^w) and specific interfacial area-saturation (a^{nw}-S^w) curves during both drainage and imbibition and found very good agreement. Then, we generated P^c-S^w-a^{nw} surfaces for

drainage and imbibition and study the conjecture developed by *Hassanizadeh and Gray* [1990, 1993].

2. Pore-Network Model

2.1. Pore Network Structure and Geometry

We develop an irregular and unstructured pore-network model. Pore bodies are represented by prolate spheroids and pore throats by tubes with n-hyperbolic polygonal cross sections (n denotes the number of vertices). Pore throat cross sections do not vary along their lengths. The topological and geometrical properties of the pore network are recovered from image analysis.

In the following parts, we present the formulations required for defining pore throat and pore body geometries.

2.1.1. Pore Throats

Cross Section Determination: Cross sections of pore throats are chosen such that the full range of shape factor, ($G = A/P^2$), calculated from image analysis, is recovered. The range of shape factor values for various cross sections is shown in Figure 1. Generally, with increasing of number of vertices, the shape factor increases as shown in Figure 1. A circle has the maximum shape factor, equal to 0.0795. For very elongated geometries (those with a small area but a large perimeter) the shape factor approaches zero.

In this study, we consider two general types for cross sections; irregular hyperbolic triangles ($n = 3$) and regular hyperbolic polygons with number of vertices $n \geq 3$ as shown in Figures 2(a) and (b), respectively. In irregular hyperbolic triangles, edges have different lengths (and radii of curvature). We consider only the case that the corner angles are zero. The range of shape factor values for various cross sections used in our network are shown

in Figure 1. We choose irregular hyperbolic triangles for shape factors less than 0.0163, and regular hyperbolic polygons otherwise. In regular hyperbolic polygons, all edges have the same length and the same radius of curvature. The corner angles are also equal and can be zero or larger (Figure 2(b)). For a given inscribed circle with radius R, by changing the corner angle, we can change the radius of curvature of edges, perimeter, area, and consequently shape factor G.

For a given cross section type, with increasing the corner angle from zero to the maximum possible value of $(\frac{n-2}{n}\pi)$, the cross section changes from a regular hyperbolic polygonal cross section to a regular polygonal cross section, and the shape factor increases. The choice of cross section type is based on the measured shape factor distribution of the pore throats acquired by image analysis. Geometrical properties and entry capillary pressures of these two general cross sections are obtained as described below.

Irregular Hyperbolic Triangles: When three circles with different radii, namely R_1, R_2, R_3 are tangential to each other, they close off a specific geometrical shape among themselves (hatched region in Figure 2(a)). This is typically the cross section of a pore throat in a granular medium. This shape can be uniquely characterized by the radius of its inscribed circle R and its shape factor G. In principle, for a desired set of values for R and G, it is possible to calculate radii R_1, R_2, R_3, and angles α, β, and γ (shown in Figure 2(a)). The required equations, derived in *Appendix A*, are given below. They constitute a set of six nonlinear coupled equations that can be solved numerically using

the *Newton-Raphson* method.

$$R = \frac{R_1 R_2 R_3}{R_1 R_2 + R_2 R_3 + R_1 R_3 + 2\sqrt{R_1 R_2 R_3 (R_1 + R_2 + R_3)}} \tag{1}$$

$$\sin\alpha = \frac{2\sqrt{R_1 R_2 R_3 (R_1 + R_2 + R_3)}}{(R_1 + R_2)(R_1 + R_3)} \tag{2}$$

$$\sin\beta = \frac{2\sqrt{R_1 R_2 R_3 (R_1 + R_2 + R_3)}}{(R_1 + R_2)(R_2 + R_3)} \tag{3}$$

$$\sin\gamma = \frac{2\sqrt{R_1 R_2 R_3 (R_1 + R_2 + R_3)}}{(R_2 + R_3)(R_1 + R_3)} \tag{4}$$

$$\alpha + \beta + \gamma = \pi \tag{5}$$

$$G = \frac{\sqrt{R_1 R_2 R_3 (R_1 + R_2 + R_3)} - 0.5(R_1^2 \alpha + R_2^2 \beta + R_3^2 \gamma)}{(R_1 \alpha + R_2 \beta + R_3 \gamma)^2} \tag{6}$$

Regular Hyperbolic Polygons (n vertices): A regular hyperbolic polygon is enclosed among three or more intersecting circles of equal radius. For example, Figure 2(b) shows a hyperbolic pentagonal cross section generated by five intersecting circles with radius R_1. A regular hyperbolic polygon is uniquely characterized by its inscribed radius R, shape factor G, and number of vertices n. Thus, for given R, G, and n, the following set of equations can be solved to determine R_1 and φ. φ is the angle between the tangent at a vertex and the line connecting the vertex to the center of the cross section.

$$G = \frac{\cos^2\varphi \cot\frac{\pi}{n} - \pi(\frac{1}{2} - \frac{1}{n}) + \varphi - 0.5\sin 2\varphi}{4n[\pi(\frac{1}{2} - \frac{1}{n}) - \varphi]^2} \tag{7}$$

$$R_1 = R\frac{\sin\frac{\pi}{n}}{\cos\varphi - \sin\frac{\pi}{n}} \tag{8}$$

Detailed explanation for the derivation of this set of equations is given in *Appendix B*. Note that for a regular polygon, $\varphi = \frac{\pi}{2} - \frac{\pi}{n}$, $R_1 = \infty$, and $G = \frac{\cot\frac{\pi}{n}}{4n}$.

2.1.2. Pore Bodies

The pore bodies are chosen to have the shape of a prolate spheroid with equatorial radii a and b, where $a \le b$ (Figure 3). The volume of a prolate spheroid is equal to $\frac{4}{3}\pi a^2 b$.

2.2. Invasion Criteria

In multiphase flow, the invasion is locally controlled by capillary pressure, i.e. the difference between nonwetting and wetting phase pressures. Pore throats control the invasion during drainage, and pore bodies during imbibition. Thus, network models require knowledge of the pore throat entry capillary pressure (for drainage), and the pore body filling capillary pressure (for imbibition).

2.2.1. Pore Throat Invasion

Figure C.1 shows the schematic cross section of a pore throat filled with nonwetting and wetting fluids. The fluid-fluid interface has a radius of curvature r_c. We denote the area occupied by the nonwetting phase by A_n and the length of contact lines between various phases by L_{ns}, L_{nw}, and L_{ws} (Figure C.1). The relationship between the entry capillary pressure (P_e^c) and geometrical parameters is found by examining force balance under equilibrium conditions (see *Appendix C*). This results in:

$$\frac{P_e^c}{\sigma^{nw}} = \frac{1}{r_c} = \frac{L_{nw} + L_{ns}\cos\theta}{A_n} \tag{9}$$

where, σ^{nw} is the interfacial tension. This equation is equally valid for regular and irregular hyperbolic polygons.

Irregular Hyperbolic Triangle: According to Equation 9, L_{nw}, L_{ns}, and A_n should be known for a given cross section, in order to calculate r_c. The formulas for calculation of these terms are given in Table D.1 based on the geometries given in Figures D.1(a) and (b). Detailed explanation for the derivation of the these formulas is given in *Appendix D*.

Substitution of L_{nw}, L_{ns}, and A_n from Table D.1 into Equation 9 results in a highly nonlinear equation for r_c involving nine other unknowns, namely ε^i, ε_i^i, ε_{i+1}^i ($i = 1, 2, 3$).

That equation, therefore, has to be supplemented with the following nine equations:

$$\tan \varepsilon_i^i = \frac{r_c \sin \varepsilon^i}{R_i \cos(\theta + \varepsilon^i)}, i = 1, 2, 3 \tag{10a}$$

$$\tan \varepsilon_{i+1}^i = \frac{r_c \sin \varepsilon^i}{R_{i+1} \cos(\theta + \varepsilon^i)}, i = 1, 2, 3 \quad (\varepsilon_4^3 = \varepsilon_1^3, R_4 = R_1) \tag{10b}$$

$$\varepsilon^i + \varepsilon_i^i + \varepsilon_{i+1}^i = \frac{\pi}{2} - \theta, i = 1, 2, 3 \quad (\varepsilon_4^3 = \varepsilon_1^3) \tag{10c}$$

Thus, Equations 9 and 10 form a set of 10 equations to be solved for r_c, ε^i, ε_i^i, and ε_{i+1}^i ($i = 1, 2, 3$). The resulting nonlinear system of equations has been solved numerically using NLEQ1S [*Nowak and Weimann*, 1991], which employs the global affine invariant Newton algorithm. Detailed explanation for the derivation of the set of equations is given in *Appendix D*. Once r_c is known, entry capillary pressure P_e^c can be calculated.

Regular Hyperbolic Polygon: Figure D.1(c) shows the vertex of a regular hyperbolic polygon filled by the wetting phase. Similar to the approach used for irregular hyperbolic triangle and according to Figures 2(b) and D.1(c), L_{nw}, L_{ns}, and A_n may be written as functions of geometrical parameters, as derived in *Appendix D* and shown in Table D.1.

Substitution of L_{nw}, L_{ns}, and A_n in Equation 9 results in a nonlinear equation for r_c involving two other unknowns, namely ε and ε'. That equation, therefore, has to be supplemented with the following two equations in order to solve for r_c, ε, and ε'.

$$\frac{\sin \varepsilon}{\sin 2(\varphi + \varepsilon')} = \frac{R_1 \sin \varepsilon'}{r_c \sin(\varepsilon + \varepsilon' + \theta)} \tag{11a}$$

$$2\varepsilon' + \varepsilon = \frac{\pi}{2} - \theta - \varphi \tag{11b}$$

We solve this set of equations numerically using standard *Newton-Raphson* method.

2.2.2. Pore Body Filling

Since the entry capillary pressure of pore bodies is smaller than that of pore throats, pore bodies are filled spontaneously under drainage. However, during imbibition they are filled gradually. For the fluid-fluid interface shown in Figure 3, assuming that the interface is normal to the equatorial radius a, we can calculate the filling capillary pressure under imbibition. Here also, Equation 9 applies. A_n and L_{ns} are given by the following formulas:

$$A_n = \pi a' b' \tag{12a}$$

$$L_{ns} \approx \pi \sqrt{2(a'^2 + b'^2)} \tag{12b}$$

where a' and b' are shown in Figure 3. Based on Equations 9 and 12, and introducing $\Gamma = a/b = a'/b'$, it follows that

$$\frac{P^c}{\sigma^{nw}} = \frac{1}{r_c} = \frac{\sqrt{2(1+\Gamma^2)}}{a'}, \quad \Gamma = \frac{a}{b} = \frac{a'}{b'} \tag{13}$$

For a given r_c and a', we can approximate volume of the wetting fluid by:

$$V_w \approx \frac{4}{3}\pi a' b' (a - \sqrt{a^2 - a'^2}) \tag{14}$$

2.3. Translation of Pore Space Data into the Pore Network

Relationships presented so far are employed in development of pore-network elements by analyzing 3-D microtomography images. We need the following information:

• Skeleton of the porous medium (connectivity information of pore bodies to pore throats)

• Pore body center coordinates and their coordination number.

- Pore unit volumes; this is the volume delineated by the narrowest cross sections of all pore throats connected to a pore body. Figure 4 shows schematically such a pore unit in two dimensions.

- Equatorial radii of pore bodies. Three principal diameters are determined for each pore unit by measuring the pore width through the centroid of pore unit in each of the principal directions. One half of the two smallest principal diameters are assigned as equatorial radii a, b of the representative prolate spheroids.

- Pore throat cross-sectional area and the corresponding shape factor. They should be determined so that the total volume of void space is conserved in the network model. Thus, length of pore throats in the pore-network model will be determined such that the volume of each and every pore-unit is the same as the volume of corresponding pore body and corresponding part of connected pore throats.

The procedure for generation of the pore-network model is as follows: In the first step, exact topology of the porous medium is translated into the pore network; i.e. skeleton of the porous medium resulted from image analysis is used to determine number of pore bodies, number of pore throats, and connectivity. Next, using a search algorithm and with sequential numbering of pore bodies and pore throats, the connectivity matrix (showing which pore body is connected to which pore throat) is generated. As a result, the coordination number distribution of the porous medium is generated in the pore network. Furthermore, in the analysis, we determine which pore throats are located on the boundary of the imaged section.

In the second step, local geometrical information is assigned to the pore network elements. The volumes of pore units are estimated by analysis of the 3-D microtomography

images using *3DMA-Rock* software. Calculated equatorial radii a and b determine the volume (Section 2.1.2) of each pore body. The difference between the pore unit volume and pore body volume (referred to as "excess volume") should be assigned to the pore throats. Excess volume of each pore unit will determined the length of pore throats located in that pore unit. Knowing the cross-sectional area of pore throats from image processing and assuming that all pore throats within a pore unit have the same length, the length of pore throats belonging to a pore unit can be determined. Finally, the total length of a pore throat is obtained by adding the two pore throat lengths from the two neighboring pore units.

As the last step, cross section geometry of each pore throat should be determined. Using the shape factor and cross sectional area of pore throats, geometry of the cross sections can be determined using the approach proposed in Section 2.1.1.

We used *3DMA-Rock* software [*Lindquist*, 2009] for image analysis. This software employs a voxel-based medial axis approach to extract topological and geometrical properties of a porous medium. Detailed information about application of this software can be found in *Prodanović et al.* [2006, 2007].

3. Case Study:Two-Phase Experiments in Packed Glass Beads

3.1. Materials and Experiments

We analyze a set of air and water displacement experiments carried out in a synthetic porous medium [*Culligan et al.*, 2004]. The medium consisted of packed soda lime glass beads with three size classes, 0.6, 0.85 and 1.0-1.4 mm in diameter. Porosity of the column was 34%. The beads were packed in a column of 7 mm in diameter and 70 mm in length.

The column was connected to the atmosphere on the top, and to a water reservoir at the bottom. Experiment specifications are shown in Table 1.

The column was packed dry and subsequently filled with water. Primary drainage, main imbibition, and main drainage experiments were performed. To prevent air from entering the water reservoir, a semi-permeable membrane was placed at the bottom of the column. Experiments were performed by pumping a known amount of water in or out of the medium. After shutting off the pump, the system was allowed to equilibrate. Then, fluid pressures were measured and a 5-mm section of the column was imaged using X-ray microtomography for each P^c-S^w point in the experiments (image voxel length was 17 μm). The three-dimensional images allowed to quantify fluids distribution and determine saturation and specific interfacial area for each equilibrium point. Water pressure was measured directly above and below the imaged section as well as in the water line outside of the column. This procedure was repeated multiple times in each cycle to obtain enough points to construct a complete drainage or imbibition curve.

3.2. Numerical Simulations

As explained before, the imaged section of glass beads was translated into the pore-network model. Figure 5(a) shows the shape factor distribution for pore throat cross sections as computed with *3DMA-Rock*. Based on this shape factor distribution, we select the cross-sectional shapes as shown in Table 2. A small range of the distribution falls outside the theoretical upper limit (0.0795). This is attributed to the finite resolution of the image and the fact that the bottlenecks between pore units are not necessarily planar surfaces. This range is represented by circles in our model. Figure 5(a) shows that the

majority of pore throats (97.2%) can be reproduced using regular hyperbolic polygonal cross sections with five vertices.

Figure 5(b) shows the coordination number distribution of the glass beads sample as computed with *3DMA-Rock*. It should be noted that the most frequent coordination numbers are 3 and 4 for this medium. There is also a coordination number of 113, which is related to a large pore in the glass beads connected to many other neighboring pores. Results of image analysis shows that there are 367 pore bodies and 1302 pore throats. Total volume of the void space is 31.85 mm^3. Out of this volume, 26.64 mm^3 are assigned to the pore bodies and 5.21 mm^3 to the pore throats.

3.2.1. Boundary Conditions

Pore throats connected to the side boundaries are closed in order to mimic the experiments. Reservoirs of fluids are each at a constant pressure. Top and bottom pore throats might be assumed to be connected to reservoirs of nonwetting fluid (air) and wetting fluid (water). As mentioned earlier, the scanned section simulated by our model is only a small part of a larger column. Since capillary forces are dominant in the experiments, there is a capillary fingering regime in the column. Thus only a few pores on the scanned column section are in contact with the invading phase reservoir. It means that our assumption for "connectivity of the boundary pores" to the nonwetting fluid reservoir is unclear. Two different assumptions for accessibility of the boundary pores might be considered: a) assuming all pores on the top boundary of the scanned section are in contact with the nonwetting fluid reservoir. b) assuming only one of more largest pores on the boundary of the scanned section are in contact with the nonwetting phase reservoir. The effect of

these assumptions on P^c-S^w and a^{nw}-S^w curves and the correct choice in this regard will be discussed in Section 4.2.

3.2.2. Simulation of Primary and Main Drainage

At the start of primary drainage, the pore network is fully saturated with the wetting phase (water). For the main drainage, the wetting phase is initially present in some pores, as determined at the end of an imbibition simulation. The pressure of the wetting phase reservoir is assumed to be zero and not changing. The pressure of the nonwetting phase reservoir is initially set to zero, and thus the imposed capillary pressure is also zero. Drainage simulation starts by increasing the pressure of the nonwetting phase reservoir to the entry capillary pressure P^c_e of the largest pore throat connected to the reservoir (Equation C1). As the entry capillary pressure of a pore body is smaller than that of a pore throat, the controlling element is the pore throat. Thus, as soon as the pressure is high enough to enter a pore throat, because the pore throat has a constant cross section, nonwetting phase would occupy that pore throat and the connected pore body. When no other pores can be occupied in that pressure step, the corresponding capillary pressure, saturation, and interfacial area are calculated. The incremental increase in nonwetting phase pressure is continued, allowing for more pores to be occupied by the nonwetting phase. Simulation of drainage scanning curves is more complex than primary drainage curve. Since each drainage scanning curve starts from an equilibrium imbibition point, fluid configuration should be captured properly. There may be some trapped nonwetting phase at the beginning of drainage scanning curve. Therefore, a search algorithm is required to determine these trapped nonwetting blobs. Invasion can happen only from

those pores which are in contact with the nonwetting reservoir, and in the process of invasion, they will connect to the trapped nonwetting phase blobs.

3.2.3. Simulation of Imbibition

The fluid configuration at the end of the primary drainage simulations is used as the starting condition for main imbibition. The pressure of nonwetting phase reservoir is decreased, causing the nonwetting phase to recede. The replacement of the nonwetting phase by the wetting phase starts from those pore throats that have the highest entry pressure (smallest size). Since there are many pore throats with angular cross sections, the wetting phase is always present in the corners. With decreasing of the capillary pressure, the wetting phase content in the corners of pore throats will increase, eventually filling the pore throat. A pore throat with a noncircular cross section will be filled completely by the wetting phase only if the following criterion is met [*Vidales et al.*, 1998].

$$P^c \leq \frac{\sigma^{nw}}{R}(\cos\theta - \sin\theta) \tag{15}$$

Where R is the radius of inscribed circle. For circular cross sections, a pore throat will be fully filled if $P^c \leq 2\frac{\sigma^{nw}}{R}\cos\theta$. Once a pore throat connected to the wetting phase reservoir is filled, the wetting phase enters the neighboring pore body and stops at a position with a curvature corresponding to the imposed capillary pressure (for which a' is calculated from Equation 13). For sake of simplicity of geometrical configurations, we assume that only one interface may exist in each pore body. As the capillary pressure is decreased further, the wetting phase gradually fills the pore body. As soon as the interface radius is equal to the pore body maximum radius (Equation 13), the rest of the pore body and the connected pore throats fill up instantaneously by the wetting phase. Similar to the

drainage experiment, for a given boundary pressure, when no other pores can be filled, capillary pressure, saturation, and interfacial area are calculated. Simulation of imbibition scanning curves is not different from main imbibition curve. The only difference is the starting wetting phase saturation.

The simulation of the full cycle of primary drainage and main imbibition took less than 2 minutes on Intel(R) CPU 6600, 2.4GHz with 2GB RAM.

3.2.4. Calculation of Saturation, Capillary Pressure and Specific Interfacial Area

Under static conditions, and in the absence of gravity, capillary pressures, P^c, at all interfaces are the same, equal to the difference between nonwetting and wetting fluid reservoir pressures, ($P^c = P^n - P^w$). Saturation of each phase can be easily calculated from the geometry and fluid occupancy of pore bodies and pore throats. We can also calculate the interfacial areas as we know the location of fluid-fluid interfaces within pore throats and pore bodies. Two different interface types may be identified: "*arc menisci* (AM)", formed along pore throat edges, and "*main terminal menisci* (MTM)", spanning the cross section of a pore body or a pore throat [*Mason and Morrow*, 1987]. The area of "AM" is calculated from total length of nonwetting-wetting phase lines and length of pore throats. Behavior of MTM during drainage and imbibition is different. During drainage, within a pore body filled with the nonwetting phase, there is MTM at the entrance of a pore throat, which is not invaded yet. Since the exact geometry of the interface is complicated, we approximate its area during drainage with that of the pore throat cross section; thus, effectively assuming a flat interface. However, during imbibition the MTM will be situated within a pore body. The area of a MTM within a prolate spheroidal pore

body can be calculated using Equation 12(a) and the volume of the wetting phase can be calculated using Equation 14.

4. Results and Discussions

4.1. Grain Size Distribution

The hyperbolic polygon shapes chosen for the pore throat cross sections in our model were characterized by semi-circular edges. In our model, radii of the edges were calculated from the shape factor distribution. The consistency of the pore-network model with the actual soil sample can be examined by comparing the calculated radii of edges and nominal grain size distribution as shown in Figure 6. The histogram distribution in Figure 6 has been generated for the three classes of grain size mentioned in the experimental data. There is a very good agreement between the model and the actual sample. This shows that generation of the cross sections in the model is consistent with grain sizes while the shape factor distribution is fully recovered from image analysis.

4.2. Effect of Boundary Pore Connectivity

As explained in Section 3.2.1, not all boundary pores are necessarily connected to the nonwetting phase reservoir. We did some simulations to analyze effect of this connectivity boundary pore(s) on P^c-S^w and a^{nw}-S^w curves. Our analysis (not presented here) shows that assuming all boundary pores connected to the nonwetting phase has a significant influence on a^{nw}-S^w curve. If all pore bodies located on the boundary are assumed to be connected to the nonwetting phase reservoir, initially there will be a significant amount of interfacial area, which is not in agreement with data. But, if we assume only few of the largest boundary pore(s) be connected to the reservoir, creation of specific interfacial

area occurs gradually as the pressure is increased. This analysis shows that the imaged section of glass-bead column is not so large to be insensitive to the boundary conditions. However, the effect of boundary condition on a^{nw}-S^w has been minimized by assuming the largest pore to be connected to the nonwetting phase reservoir.

4.3. Effect of Shape Factor and Pore Shape on P^c, S^w, and a^{nw}

As mentioned in Section 1, up to now only shape factor (G) has been introduced in the development of pore-network models. But, geometrical shape (number of vertices n) and shape factor (G) are the two parameters that control the entry capillary pressure (P_e^c), (corner) wetting phase saturation $(ş^w)$, and specific interfacial area $(ą^{nw})$ associated with arc menisci (AM). These effects are illustrated for a single pore throat as well as for the whole network.

First, effects of n and G on entry capillary pressure, corner wetting phase saturation, and AM area for a single pore are shown. We consider a number of pore throats with a unit length, and the same cross-sectional area (A_{tot}). All pores have regular hyperbolic polygon shape with different values for G and n. Corner saturation is defined as the ratio of cross-sectional area of wetting phase to total cross-sectional area of a pore throat, A_w/A_{tot}. Figures 7(a) and 7(b) show variations of the corner saturation $(ş^w)$ as a function of shape factor (G) and number of vertices (n) for two different situations, $r_c = 0.5R_{eq}$, and $r_c = 0.15R_{eq}$, respectively. R_{eq} is defined as the radius of a circle with area of A_{tot}, i.e. $R_{eq} = \sqrt{A_{tot}/\pi}$. These figures show that $ş^w$ strongly depends on G and n. This dependence, however, decreases as G and/or n increase. At larger capillary pressures $(r_c = 0.15R_{eq})$, there is a non-monotonic dependence. As the number of vertices increases, more wetting phase can be kept in the corners (larger $ş^w$) for a given shape factor. In

both cases, for large number of vertices, $\mathrm{\textit{s}}^w$ approaches zero because the cross section approaches a circle.

Although in this work the geometries of pore throats' cross sections have been idealized, these results may illustrate the origin of uncertainties in some applications of predictive pore-network models. If in a real porous medium the volume of pore throats compared with pore bodies is considerable, shape of the cross section can influence the accuracy of quantitative assessment. For instance, while in all simulations shown in Figure 7, cross section areas are the same, residual wetting phase saturations are significantly different for a given shape factor. This effect can be even more significant for quantitative assessment of relative permeability curves, where $k^\alpha \propto S^\alpha$. As Figure 7 shows at small capillary pressures (high wetting phase saturation), effect of shape of cross sections is important. Simulations of relative permeabilities using pore-network models show that the largest inaccuracies occur at high saturations, especially for the wetting phase permeability [e.g. *Blunt et al.*, 2002; *Valvatne and Blunt*, 2004]. This implies that for predictive pore-network modeling, in addition to G, the number of vertices (n) should be included in the development of pore networks.

Fluid-fluid interfacial area in a pore throat contributes to the AM area. For a single pore throat, effect of G and n on AM is investigated by examining $\mathrm{\textit{a}}^{nw}$, defined as the ratio of the length of nonwetting-wetting line (L_{nw}) to the total cross-sectional area, A_{tot}. Variations of $\mathrm{\textit{a}}^{nw}$ with G and n for $r_c = 0.5 R_{eq}$ is shown in Figures 8(a). As it can be observed, $\mathrm{\textit{a}}^{nw}$ varies monotonically with G values and increases as the number of vertices increases. With increase of capillary pressure (decrease of r_c), corner specific interfacial area decreases. Our analysis (not presented here) shows that with the increase of P^c by a

factor of three, the specific interfacial area decreases by about half. Effect of geometrical shape and shape factor on specific interfacial area will be important in those porous media that have long pore throats. In such porous media, AM area can be even smaller that AM area. This has been shown by *Raeesi and Piri* [2009]; depending on the geometry and topology of a porous medium, interfacial area associated with the arc menisci can be larger than the interfacial area associated with the area of MTM. *Raeesi and Piri* [2009] have simulated AM and MTM area in two mixed cross-sectional pore-network models based on *Berea* sandstone and *Saudi Aramco* sandstone, and show that the area of AM is larger than the area of MTM.

Finally, the effect of G and n on entry capillary pressure for a single pore throat is shown in Figure 8(b). Here, entry capillary pressures have been normalized with the entry capillary pressure for a circular tube with the same cross-sectional area (A_{tot}). It is evident that the entry capillary pressure decreases monotonically with the increase in G and/or n. Obviously, as the number of vertices increases, the entry capillary pressure approaches that of a circular cross section.

To see the effect of shape of cross section on macroscale P^c-S^w and a^{nw}-S^w curves, we have simulated drainage experiments with three different networks consisting of circular cross sections, mixed polygonal cross sections, and mixed hyperbolic polygonal cross sections. Figures 9(a) and 9(b) show P^c-S^w and a^{nw}-S^w curves, respectively, compared to the experimental data. It is obvious that including the hyperbolic polygonal cross section significantly improves the agreement between simulations and experiments, especially for P^c-S^w curves.

In simulations shown in Figure 9, all networks have the same skeleton (coordination number distribution), void volume, and pore throat cross sectional area distribution. Since the network is small (364 pore bodies), effect of pore geometries are pronounced. A network with all pores having circular cross sections cannot recover the shape factor distribution. So, for a given cross-sectional area, it results in a smaller entry capillary pressure than the other shapes. In addition, there is no saturation associated with the wetting phase in the corners. The difference between results for a mixed polygonal network and mixed hyperbolic polygonal network for large saturations is not significant. However, at small saturations, smallest pores need to be invaded. Obviously for high capillary pressures, a network with hyperbolic polygonal cross sections can keep more wetting phase in the corners compared with other types of networks. Effect of n on the specific interfacial area values over the whole domain is not very significant. This is because in glass beads, the volume of pore throats compared with the volume of pore bodies is not significant. Thus, area of AM is much smaller than the area of MTM.

4.4. P^c-S^w and a^{nw}-S^w Curves

We employ insights obtained from the study of effects of boundary pores and cross section geometry to simulate the experimental data. Thus, P^c-S^w and a^{nw}-S^w curves have been obtained for primary drainage and main imbibition processes using a network with mixed hyperbolic polygonal pore throats and a single pore connected to the boundary. Results are shown in Figures 10(a) and 10(b). The agreement with measured curves are excellent. This is a particularly significant result for imbibition curves as many pore-network models have had difficulty to match imbibition data points for capillary pressure.

Figure 10(a) shows that there is a strong hysteresis in P^c-S^w curves resulted from drainage and imbition (up to 100%). The magnitude of this hysteresis is larger than that of P^c-S^w curves resulted from sand pack columns [*Valvatne and Blunt*, 2004]; which is due to the larger aspect ratio of pores in glass bead packing.

Compared with P^c-S^w curves, there is more discrepancies between a^{nw}-S^w curves especially during imbition. This is due to the small size of the domain and simplified geometries assumed for the interface. Nevertheless, accuracy of the model in prediction of a^{nw} is good. Such model can be a powerful tool for generating input data such as P^c-S^w-a^{nw} surface needed for new macroscopic multiphase flow simulators such as *Niessner and Hassanizadeh* [2008, 2009]. They solved multiphase flow and transport equations including interfacial area as a new state variable.

4.5. P^c-S^w-a^{nw} Surfaces

After having validated the model against experimental data, we can use it to investigate role of specific interfacial area in removing or reducing the hysteresis in capillary pressure-saturation curves. We have simulated many scanning loops of drainage and imbition and have calculated equilibrium values of P^c, S^w, and a^{nw}. Results are plotted in Figures 11(a) and (b) for drainage and imbition, respectively, where contours of a^{nw} are shown in P^c-S^w plane. The shade coding shows specific interfacial area for a given pair of capillary pressure and saturation. The natural neighbor interpolation method [*Sibson*, 1981] has been used to generate the surfaces. The corresponding surfaces have been depicted in Figures 11(a) and (b) by showing contour lines of equal specific interfacial area. The correlation coefficient between the two surfaces was found to be 95%. Next, the difference between imbition and drainage surfaces has been normalized by drainage

surface as plotted in Figure 11(c). As it can be observed, the maximum difference in main loop of drainage and imbibition curves is about 25%. The average normalized difference over the entire surface is about 15%. To investigate in more detail causes of difference between drainage and imbibition surfaces, we have included normalized difference between experimental data and simulations (Figure 11(d)). The average normalized difference in this figure is 19%, which is very close to the average difference calculated in Figure 11(c) with similar spatial trend in error variation. We should note that the maximum difference is observed in the range of capillary pressure-saturation where no data point exists. Thus, it could be mainly an artifact of the interpolation. A similar trend was found by *Joekar-Niasar et al.* [2009] (Figure 12c, page 10), which was also due to lack of imbibition data points in that region. Comparing Figure 11(c) with 11(d), one can observe that the difference between the simulated drainage and imbibition surfaces is very close to the uncertainty range of modeling procedure.

The maximum differences in P^c-S^w and a^{nw}-S^w curves in micro-model simulations of *Joekar-Niasar et al.* [2009] were about 20% and 300%, respectively. None of these values are common in real three-dimensional porous media. Nevertheless, the reduction in difference between $a^{nw} = f(P^c, S^w)$ surfaces over the whole loop of drainage and imbibition ($S^w \in [0.65, 1]$) was considerable [*Joekar-Niasar et al.*, 2009]. In this work, the maximum differences between P^c-S^w and a^{nw}-S^w curves (i.e. the hysteresis effect) are 100% and 50%, respectively. Whereas, the difference between $a^{nw} = f(P^c, S^w)$ surfaces over the whole loop of drainage and imbibition ($S^w \in [0.15, 1]$) is about 15%. This is a major reduction of hysteretic behavior. Thus, we can conclude that $a^{nw} = f(P^c, S^w)$ surfaces are almost identical within experimental and computational uncertainties; i.e. the hysteresis

in P^c-S^w-a^{nw} surfaces for the main loop is negligible. One should note that these results are related to a three-dimensional unstructured and irregular porous medium, which is topologically and geometrically very different from previous works such as *Reeves and Celia* [1996]; *Held and Celia* [2001]; *Joekar-Niasar et al.* [2008, 2009].

5. Summary and Conclusions

One of the goals of the study has been to determine whether shape factor alone is enough to characterize the pore geometry of a granular porous medium. In particular, the role of actual shape of pores is investigated.

In this paper, a geometry-based approach has been proposed for generation of pore throat cross sections so that the whole range of shape factor distribution can be reproduced. Three different general shapes for pore throats have been considered: irregular hyperbolic triangles, regular hyperbolic polygons, and circles. General formulas for calculation of geometrical properties and entry capillary pressure of these geometries are derived. Effects of shape factor as well as cross-sectional shape on entry capillary pressure, corner saturation and corner interfacial area have been investigated for a single pore throat. We have shown that in addition to shape factor, the shape of cross section (number of vertices) has a significant effect on entry capillary pressure, corner saturation, and arc menisci area. These parameters can be very important in porous media with long pore throats and may contribute significantly to the total pore volume.

We have developed an irregular unstructured mixed cross-sectional pore-network model, with the pore bodies in the shape of prolate spheroids and pore throats having a mix of cross sectional shapes described above. The model has been used for simulating drainage and imbibition experiments carried out by *Culligan et al.* [2004] in a glass-bead column.

The capability of the pore-network model for simulating a real porous medium has been successfully verified, as we reproduce the measured P^c-S^w and a^{nw}-S^w curves very well. Moreover, grain size distribution inferred from our pore-network model is in close agreement with the measured distribution. We have shown that the inclusion of shape factor distribution and cross-sectional shape in the generation of pore network significantly influence P^c-S^w curves. Depending on the number of vertices of a cross section and volume and length associated with the pore throats, shape factor distribution and cross-sectional shape can significantly influence a^{nw}-S^w curves.

Another goal of this work is to investigate the role of specific interfacial area in reducing the hysteresis in P^c-S^w curves for a real porous medium. Using this pore-network model, we have generated P^c-S^w-a^{nw} surfaces for drainage and imbibition, separately. Comparison between these two surfaces shows that they are highly correlated ($r^2 = 0.95$), and the normalized difference is small, in the range of uncertainty of model calculations. Our results show that in glass beads with unstructured irregular network with mixed cross sections, the hysteresis in P^c-S^w-a^{nw} curves is much smaller than the hysteresis in P^c-S^w curves. The largest relative error between $a^{nw} = f(P^c, S^w)$ surfaces is found at large saturations, where the specific interfacial area is very small. Finally, we emphasize that the proposed approach for generating pores cross sections, based on the continuous recovery of shape factor distribution, is essential for the development of predictive pore-network models.

Appendix A: Irregular Hyperbolic Triangle Geometry

For a set of *Soddy circles* shown in Figure 2(a), the inscribed radius, R, can be determined based on the radii of the three tangent circles.

$$R = \frac{R_1 R_2 R_3}{R_1 R_2 + R_2 R_3 + R_1 R_3 + 2\sqrt{R_1 R_2 R_3 (R_1 + R_2 + R_3)}} \tag{A1}$$

The area of the $\triangle ABC$ may be written as follows:

$$A_{\triangle ABC} = \sqrt{R_1 R_2 R_3 (R_1 + R_2 + R_3)} \tag{A2}$$

On the other hand, using laws of sines in $\triangle ABC$, we can write the following three equations:

$$\frac{R_1 + R_2}{\sin \gamma} = \frac{R_2 + R_3}{\sin \alpha} = \frac{R_1 + R_3}{\sin \beta} = \frac{(R_1 + R_2)(R_2 + R_3)(R_1 + R_3)}{2\sqrt{R_1 R_2 R_3 (R_1 + R_2 + R_3)}}$$

$$\alpha + \beta + \gamma = \pi \tag{A3}$$

The area and perimeter of the irregular hyperbolic triangle, the hatched part of Figure 2(a), is denoted by as $A_{hatched}$ and $P_{hatched}$, respectively. They can be written:

$$A_{hatched} = \sqrt{R_1 R_2 R_3 (R_1 + R_2 + R_3)} - 0.5(R_1^2 \alpha + R_2^2 \beta + R_3^2 \gamma) \tag{A4}$$

$$P_{hatched} = R_1 \alpha + R_2 \beta + R_3 \gamma \tag{A5}$$

Finally, the shape factor, G, can be calculated, as:

$$G = \frac{\sqrt{R_1 R_2 R_3 (R_1 + R_2 + R_3)} - 0.5(R_1^2 \alpha + R_2^2 \beta + R_3^2 \gamma)}{(R_1 \alpha + R_2 \beta + R_3 \gamma)^2} \tag{A6}$$

For given values of G and R, we can solve Equations A1,A3 and A6 numerically, using *Newton-Raphson* method, to calculate $R_1, R_2, R_3, \alpha, \beta$, and γ.

Appendix B: Regular Hyperbolic Polygon Geometry

To relate the shape factor to geometry of a cross section, the area and perimeter should be calculated. The area of the n-hyperbolic polygon $(B_1..B_n)$ in Figure 2(b) can be calculated as follows:

$$A_{B_1..B_n} = A_{A_1..A_n} - n \times A_{\triangle A_1 A_2 B_1} - n \times A_{\lhd A_2 B_1 B_2} \tag{B1}$$

Because $\angle A_2 B_1 O = \pi/2 + \varphi$ and $\phi = \pi/n$, we obtain:

$$\beta = \pi\left(\frac{1}{2} - \frac{1}{n}\right) - \varphi \tag{B2}$$

In addition, we note that $\tan \phi = \tan \frac{\pi}{n} = \frac{R_1 \sin \beta}{R + R_1(1 - \cos \beta)}$, which results in:

$$R_1 = R\frac{\sin \frac{\pi}{n}}{\cos \varphi - \sin \frac{\pi}{n}} \tag{B3}$$

The area of a n-polygon, with edge length s is:

$$A_{A_1..A_n} = \frac{n}{4}s^2 \cot \pi/n = nR_1^2 \cos^2 \varphi \cot \frac{\pi}{n} \tag{B4}$$

and the areas of $\triangle A_1 A_2 B_1$ and $\lhd A_2 B_1 B_2$ may be written as follows, respectively:

$$A_{\triangle A_1 A_2 B_1} = 0.5 R_1^2 \sin 2\varphi \tag{B5}$$

$$A_{\lhd A_2 B_1 B_2} = R_1^2 \beta \tag{B6}$$

Using Equations B3, B4, B5, and B6, Equation B1 may be written as:

$$A_{B_1..B_n} = \frac{nR^2 \sin^2 \frac{\pi}{n}}{(\cos \varphi - \sin \frac{\pi}{n})^2} \left[\cos^2 \varphi \cot \frac{\pi}{n} - \pi\left(\frac{1}{2} - \frac{1}{n}\right) + \varphi - 0.5 \sin 2\varphi\right]. \tag{B7}$$

Then, the perimeter of a n-hyperbolic polygon is obtained from:

$$P_{B_1..B_n} = 2nR\frac{\sin \frac{\pi}{n}}{\cos \varphi - \sin \frac{\pi}{n}}\left[\pi\left(\frac{1}{2} - \frac{1}{n}\right) - \varphi\right] \tag{B8}$$

Based on Equations B7 and B8, the shape factor can be written as follows:

$$G = \frac{A}{P^2} = \frac{\cos^2 \varphi \cot \frac{\pi}{n} - \pi(\frac{1}{2} - \frac{1}{n}) + \varphi - 0.5 \sin 2\varphi}{4n[\pi(\frac{1}{2} - \frac{1}{n}) - \varphi]^2} \tag{B9}$$

For given values of n and G, Equation B9 can be solved numerically to calculate φ and subsequently the geometry of the cross section will be define from Equation B3.

Appendix C: Balance of Forces for an Invading Interface

Calculation of entry capillary pressure for various cross sections is based on the MS-P (*Mayer-Stowe-Princen*) method, suggested by *Mayer and Stowe* [1965]; *Princen* [1969a, b, 1970]; *Ma et al.* [1996], which follows from the balance of forces for contact lines. When the nonwetting phase invades a tube with an angular cross section, the wetting phase remains behind in the corners along the tube. The longitudinal curvature of the resulting fluid-fluid interface inside the tube is zero. For a regular hyperbolic polygonal cross section, let radius of curvature of the interface within the cross section be denoted by r_c (see Figure C.1). Then, the entry capillary pressure is equal to:

$$P_e^c = P^n - P^w = \frac{\sigma^{nw}}{r_c} \tag{C1}$$

in which, P^n is pressure of the nonwetting phase, and P^w is the pressure of the wetting phase.

Now, consider an *nw*-interface formed at the entrance of the tube. This interface will move into the tube (i.e. nonwetting phase invades the tube) only if the entry capillary pressure given by Equation C1 is reached. At that instance, the following balance of forces for the interface can be written:

$$(P^n - P^w)A_n = L_{nw}\sigma^{nw} + L_{ns}\sigma^{ns} - L_{ns}\sigma^{ws} \tag{C2}$$

where A_n is that part of a cross section filled with nonwetting phase, L_{ns} is the total length of solid-fluid-fluid contact line, L_{nw} is the total length of arc cut through the fluid-fluid interface in the corners.

From Young equation, we have the following relationship:

$$\sigma^{ns} = \sigma^{nw} cos\theta + \sigma^{ws} \tag{C3}$$

Substituting Equation C3 in Equation C2 will result in:

$$(P^n - P^w)A_n = \sigma^{nw}(L_{nw} + L_{ns}\cos\theta) \tag{C4}$$

Combination of Equations C1 and C4 results in:

$$\frac{L_{nw} + L_{ns}\cos\theta}{A_n} = \frac{1}{r_c} \tag{C5}$$

In Equation C5, L_{nw} and L_{ns} depend on cross-sectional geometry and also fluid occupancy. Geometrical relationships between these terms and r_c should be calculated for each cross-sectional group separately as shown in Section 2.2.1.

Appendix D: Calculation of Entry Capillary Pressure for a Pore Throat
D1. Irregular Hyperbolic Polygonal Cross Sections

Consider the vertex i of an irregular hyperbolic triangle filled by the wetting phase, shown in Figure D.1. We need to calculate the area of the wetting phase in the corner as well as the length of nonwetting-wetting interface. Let ε_j^i denote the angle made by the tangent at vertex i and line connecting vertex i to the intersection of interface with edge j (e.g. line BN or BN' in Figure D.1). Also, let ε^i denote the angle between the tangent to the interface at its intersection with the edge i and the line connecting both ends of

the interface (line NN' in Figure D.1). Then in the triangle $\triangle BNN'$, we can write:

$$\varepsilon^i + \varepsilon^i_1 + \varepsilon^i_2 = \frac{\pi}{2} - \theta, (i = 1, 2, 3) \tag{D1}$$

, where θ is the fluid-fluid-solid contact angle.

Based on law of sines, we have:

$$\frac{\overline{BN}}{\sin(\varepsilon^i + \varepsilon^i_2 + \theta)} = \frac{\overline{BN'}}{\sin(\varepsilon^i + \varepsilon^i_1 + \theta)} = \frac{\overline{NN'}}{\sin(\varepsilon^i_1 + \varepsilon^i_2)} \tag{D2}$$

Radii of arcs BN, BN', and NN are R_1, R_2, and r_c, respectively. Since angles $\angle N'ON$, $\angle ABN$, and $\angle BA'N'$ are denoted by ε^i, ε^i_1, ε^i_2, respectively, we may rewrite Equation D2, as follows:

$$R_1 \tan \varepsilon^i_1 = R_2 \tan \varepsilon^i_2 = \frac{r_c \sin \varepsilon^i}{\cos(\theta + \varepsilon^i)}, i = 1, 2, 3 \tag{D3}$$

Now, the area of the wetting phase (hatched part in Figure D.1(b)) should be calculated. That is equal to the area of the triangle BNN' minus the total areas of the circular segments created by chords BN, BN', and NN', denoted by A^{cs}_{BN}, $A^{cs}_{BN'}$, $A^{cs}_{NN'}$, respectively:

$$A^i_w = A_{\triangle BNN'} - A^{cs}_{BN} - A^{cs}_{BN'} - A^{cs}_{NN'} \tag{D4}$$

With some manipulation, we can write the following equation for A^i_w.

$$A^i_w = 2r_c R_1 \sin \varepsilon^i \sin \varepsilon^i_1 \cos \varepsilon^i_2 \; - R^2_1(\varepsilon^i_1 - 0.5 \sin 2\varepsilon^i_1)$$

$$- R^2_2(\varepsilon^i_2 - 0.5 \sin 2\varepsilon^i_2)$$

$$- r^2_c(\varepsilon^i - 0.5 \sin 2\varepsilon^i) \tag{D5}$$

Next, the area of that part of pore throat cross section filled by the nonwetting phase (A_n in Figure D.1) can be calculated by subtracting the total wetting phase area from the

pore cross-sectional area (given by Equation A4), $A_{hatched}$:

$$A_n = A_{hatched} - \sum_{i=1}^{3} A_w^i \tag{D6}$$

Total length of the nonwetting-wetting interface, L_{nw}, would be estimated simply as follows:

$$L_{nw} = 2r_c \sum_{i=1}^{3} \varepsilon^i \tag{D7}$$

Using Equation A5 and considering the geometry given in Figure D.1, the length of the nonwetting-solid interface can be calculated.

$$L_{ns} = R_1\alpha + R_2\beta + R_3\gamma - 2\sum_{i=1}^{3}\left(R_i\varepsilon_i^i + R_i\varepsilon_i^{i-1}\right), \varepsilon_1^0 = \varepsilon_1^3 \tag{D8}$$

Substituting Equations D6, D7, and D8 in Equation C5 results in a new equation, which relates all $\varepsilon_j^i | i = 1, 2, 3, j = 1, 2$ and $\varepsilon^i | i = 1, 2, 3$ to the radius of curvature of the interface r_c. Te resulting equation, together with Equations D1 and D3, can be solved numerically to calculate r_c. Subsequently, it is possible to calculate the entry capillary pressure from Equation C1.

D2. Regular Hyperbolic Polygonal Cross Sections

The procedure for calculation of entry capillary pressure for a regular hyperbolic polygonal cross section, is similar to the method used for regular hyperbolic polygonal cross sections. There are few differences in geometry that should be taken into consideration. Considering Figure D.1(c), since the geometry is regular, $R_1 = R_2 = .. = R_n$. Therefore, all $\varepsilon_j^i = \varepsilon'$, $(j = 1, 2, i = 1, 2, .., n)$ are equal and denoted by ε'. In addition, $\angle NBN'$ in Figure D.1(c) will be equal to $2(\varepsilon' + \varphi)$. The angle ε' is referred to the angle made by the tangent at a vertex and line connecting the vertex to the intersection of interface and

edge. For $\triangle BNN'$ we can write $2\varepsilon' + \varepsilon = \frac{\pi}{2} - \theta - \varphi$. Based on the law of sines in $\triangle BNN'$ we may write:

$$\frac{r_c \sin \varepsilon}{\sin 2(\varphi + \varepsilon')} = \frac{R_1 \sin \varepsilon'}{\sin(\varepsilon + \varepsilon' + \theta)}, \quad 2\varepsilon' + \varepsilon = \frac{\pi}{2} - \theta - \varphi \tag{D9}$$

Next, for the area of the wetting phase, A_w^i, we can write:

$$A_w^i = 2r_c R_1 \sin \varepsilon \sin \varepsilon' \cos(\varepsilon' + \varphi) \ -2R_1^2(\varepsilon' - 0.5 \sin 2\varepsilon')$$

$$-r_c^2(\varepsilon - 0.5 \sin 2\varepsilon) \tag{D10}$$

Knowing the area of a regular hyperbolic cross section from Equation B7, $A_{B_1..B_n}$, the area of the nonwetting phase in this cross section can be calculated as follows:

$$A_n = A_{B_1..B_n} - nA_w^i \tag{D11}$$

The total length of the nonwetting-wetting interface, L_{nw} , is simply given by:

$$L_{nw} = 2nr_c\varepsilon \tag{D12}$$

According to Equation B8, the total length of L_{ns} is given by:

$$L_{ns} = P_{B_1..B_n} - 4nR_1\varepsilon' \tag{D13}$$

Substituting Equations D11, D12, and D13 in Equation C5 results in a new equation, which relates ε' and ε to the radius of curvature of the interface r_c. The resulting equation and Equation D9 can be solved numerically to calculate r_c. Finally, the entry capillary pressure is calculated from Equation C1.

References

Ahrenholz, B., J. Tölke, P. Lehmann, A. Peters, A. Kaestner, M. Krafczyk, and W. Durner (2008), Prediction of capillary hysteresis in a porous material using lattice-boltzmann methods and comparison to experimental data and a morphological pore network model, *Advances in Water Resources*, *31*(9), 1151–1173, doi:DOI: 10.1016/j.advwatres.2008.03.009.

Bakke, S., and P.-E. Øren (1997), 3-d pore-scale modelling of sandstones and flow simulations in the pore networks, *SPE Journal*, *2*(2), 136–149.

Blunt, M., M. D. Jackson, M. Piri, and P. H. Valvatne (2002), Detailed physics, predictive capabilities and macroscopic consequences for pore-network models of multiphase flow, *Advances in Water Resources*, *25*, 1069–1089.

Blunt, M. J. (2001), Flow in porous media - pore-network models and multiphase flow, *Current Opinion Colloid Interface Sci.*, *6*, 197–207.

Celia, M. A., P. C. Reeves, and L. A. Ferrand (1995), Recent advances in pore scale models for multiphase flow in prous media, *Reviews of Geophysics*, *33 (S1)*, 1049–1058.

Culligan, K. A., D. Wildenschild, B. S. B. Christensen, W. Gray, M. L. Rivers, and A. F. B. Tompson (2004), Interfacial area measurements for unsaturated flow through a porous medium, *Water Resources Research*, *40*, W12,413, doi:10.1029/2004WR003278.

Dahle, H. K., and M. A. Celia (1999), A dynamic network model for two-phase immiscible flow, *Computational Geosciences*, *3*, 1–22.

Dias, M. M., and A. C. Payatakes (1986), Network models for two-phase flow in porous media part 1. immiscible microdisplacement of non-wetting fluids, *J. Fluid Mechanics*, *164*, 305–336.

Fatt, I. (1956), The network model of porous media, i. capillary pressure characteristics, *Petroleum Trans. AIME*, *207*, 144–159.

Hassanizadeh, S. M., and W. G. Gray (1990), Mechanics and thermodynamics of multiphase flow in porous media including interphase boundaries, *Adv. Water Resour.*, *13*, 169–186.

Hassanizadeh, S. M., and W. G. Gray (1993), Thermodynamic basis of capillary pressure in porous media, *Water Resources Research*, *29*, 3389–3405.

Held, R. J., and M. A. Celia (2001), Modeling support of functional relationships between capillary pressure, saturation, interfacial area and common lines, *Advances in Water Resources*, *24*, 325–343.

Joekar-Niasar, V., S. Hassanizadeh, and A. Leijnse (2008), Insights into the relationships among capillary pressure, saturation, interfacial area and relative permeability using pore-network modeling, *Transport in Porous Media*, *74*(2), 201–219.

Joekar-Niasar, V., S. M. Hassanizadeh, L. J. Pyrak-Nolte, and C. Berentsen (2009), Simulating drainage and imbibition experiments in a high-porosity micromodel using an unstructured pore network model, *Water Resources Research*, *45*, W02,430, doi: 10.1029/2007WR006641.

Kaestner, A., E. Lehmann, and M. Stampanoni (2008), Imaging and image processing in porous media research, *Advances in Water Resources*, *31*(9), 1174–1187, doi:DOI: 10.1016/j.advwatres.2008.01.022.

Koplik, J., and T. J. Lasseter (1985), Two-phase flow in random network models of porous media, *Society of Petroleum Engineers Journal*, *25*, 89–110, doi:10.2118/11014-PA.

Lindquist, W. B. (2009), 3dma-rock, a software package for automated analysis of pore rock structure in 3d computed microtomography images.

Ma, S., G. Mason, and N. R. Morrow (1996), Effect of contact angle on drainage and imbibition in regular polygonal tubes, *Colloids and Surfaces A.*, *117*, 273–291.

Man, H. N., and X. D. Jing (2000), Pore network modelling of electrical resistivity and capillary pressure characteristics, *Transport in Porous Media*, *41*(3), 263–285, doi: 10.1023/A:1006612100346.

Mason, G., and N. R. Morrow (1987), Meniscus configurations and curvatures in non-axisymmetric pores of open and closed uniform cross section, *Proceedings of the Royal Society of London. Series A, Mathematical and Physical Sciences*, *414*(1846), 111–133.

Mason, G., and N. R. Morrow (1991), Capillary behavior of a perfectly wetting liquid in irregular triangular tubes, *J. Colloid Interface Sci.*, *141*, 262–274.

Mayer, R. P., and R. A. Stowe (1965), Mercury porosimetry-breakthrough pressure for penetration between packed spheres, *J. Colloid Sci.*, *20*, 891–911.

Mogensen, K., and E. H. Stenby (1998), A dynamic two-phase pore-scale model for imbibition, *Transport in Porous Media*, *32*, 299–327.

Niessner, J., and S. M. Hassanizadeh (2008), A model for two-phase flow in porous media including fluid-fluid interfacial area, *Water Resour. Res.*, *44*, W08,439, doi: 10.1029/2007WR006721.

Niessner, J., and S. M. Hassanizadeh (2009), Modeling kinetic interphase mass transfer for two-phase flow in porous media including fluid–fluid interfacial area, *Transport in*

Porous Media, *80*(2), 329–344, doi:10.1007/s11242-009-9358-5.

Nordhaug, H. F., M. Celia, and H. K. Dahle (2003), A pore network model for calculation of interfacial velocities, *Advances in Water Resources*, *26*, 1061–1074.

Nowak, U., and L. Weimann (1991), *A family of Newton codes for systems of highly nonlinear equations*, Konrad-Zuse-Zentrum für Informationstechnik Berlin.

Øren, P. E., and S. Bakke (2002), Process based reconstruction of sandstones and prediction of transport properties, *Transport in Porous Media*, *46*(2), 311–343, doi: 10.1023/A:1015031122338.

Patzek, T. W. (2001), Verification of a complete pore network simulator of drainage and imbibition, *SPE Journal*, *6*, 144–156.

Piri, M., and M. J. Blunt (2005), Three-dimensional mixed-wet random pore-scale network modeling of two- and three-phase flow in porous media. i. model description, *Phys. Rev. E*, *71*(2), 026,301, doi:10.1103/PhysRevE.71.026302.

Porter, M. L., M. G. Schaap, and D. Wildenschild (2009), Lattice-boltzmann simulations of the capillary pressure-saturation-interfacial area relationship for porous media, *Advances in Water Resources*, *32*(11), 1632 – 1640, doi:DOI: 10.1016/j.advwatres.2009.08.009.

Princen, H. M. J. (1969a), Capillary phenomena in assemblies of parallel cylinders i.capillary rise between two cylinders, *Colloid Interface Sci.*, *30*, 69–75.

Princen, H. M. J. (1969b), Capillary phenomena in assemblies of parallel cylinders ii.capillary rise in systems with more than two cylinders, *Colloid Interface Sci.*, *30*, 359–371.

Princen, H. M. J. (1970), Capillary phenomena in assemblies of parallel cylinders iii.liquid columns between horizontal parallel cylinders, *Colloid Interface Sci.*, *34*, 171–184.

Prodanović, M., W. B. Lindquist, and R. S. Seright (2006), Porous structure and fluid partitioning in polyethylene cores from 3d x-ray microtomographic imaging, *Journal of Colloid and Interface Science*, *298*, 282–297.

Prodanović, M., W. B. Lindquist, and R. S. Seright (2007), 3d image-based characterization of fluid displacement in a berea core, *Advances in Water Resources*, *30*, 214–226, doi:10.1016/j.advwatres.2005.05.015.

Raeesi, B., and M. Piri (2009), The effects of wettability and trapping on relationships between interfacial area, capillary pressure and saturation in porous media: A pore-scale network modeling approach, *Journal of Hydrology*, doi:10.1016/j.jhydrol.2009.07.060.

Raoof, A., and S. Hassanizadeh (2009), A new method for generating pore-network models of porous media, *Transport in Porous Media*, doi:10.1007/s11242-009-9412-3.

Reeves, P. C., and M. A. Celia (1996), A functional relationship between capillary pressure, saturation, and interfacial area as revealed by a pore-scale network model, *Water Resources Research*, *32*, 2345–2358.

Ryazanov, A. V., M. I. J. van Dijke, and K. S. Sorbie (2009), Two-phase pore-network modelling: Existence of oil layers during water invasion, *Transport in Porous Media*, *80*(1), 79–99.

Schaap, M. G., M. L. Porter, B. S. B. Christensen, and D. Wildenschild (2007), Comparison of pressure-saturation characteristics derived from computed tomography and lattice boltzmann simulations, *Water Resour. Res.*, *43*, W12S06, doi:10.1029/2006WR005730.

Table 1.   Specifications of air-water experiments in glass beads.

Property	Value	Unit
Porosity	0.34	
Sample height (imaged section)	6.1×10^{-3}	m
Sample diameter	6.9×10^{-3}	m
Water dynamic density	1.002×10^{-3}	Pa.s
Air dynamic density	1.86×10^{-6}	Pa.s
Air-water interfacial tension (σ^{nw})	0.7275	N/m
contact angle (θ)	$0 - 4$	degree

Shan, X., and H. Chen (1994), Simulation of nonideal gases and liquid-gas phase transitions by the lattice boltzmann equation, *Phys. Rev. E*, *49*(4), 2941–2948, doi: 10.1103/PhysRevE.49.2941.

Sholokhova, Y., D. Kim, and W. B. Lindquist (2009), Network flow modeling via lattice-boltzmann based channel conductance, *Advances in Water Resources*, *32*(2), 205–212, doi:10.1016/j.advwatres.2008.10.016.

Sibson, R. (1981), A brief description of natural neighbor interpolation, in *Interpolating multivariate data*, chap. 2, pp. 21–36, John Wiley & Sons, New York.

Valvatne, P. H., and M. J. Blunt (2004), Predictive pore-scale modeling of two-phase flow in mixed wet media, *Water Resour. Research*, *40*, W07,406, doi:10.1029/2003WR002627.

Vidales, A. M., J. L. Riccardo, and G. Zgrabli (1998), Pore-level modelling of wetting on correlated porous media, *J. Phys. D, Appl. Phys.*, *31*, 2861–2868.

Wildenschild, D., J. W. Hopmans, C. M. P. Vaz, M. L. Rivers, and D. Rikard (2002), Using x-ray computed tomography in hydrology: Systems, resolutions, and limitations, *J. Hydrology*, *267*, 285–297.

Table 2.   Classification of cross sections based on the shape factor distribution.

Zone	Shape Factor (G)	Cross Section
1	$G < 0.0163$	irregular hyperbolic triangle (3 vertices)
2	$0.0163 \leq G < 0.0217$	regular hyperbolic triangle (3 vertices)
3	$0.0217 \leq G < 0.0244$	regular hyperbolic polygon (4 vertices)
4	$0.0244 \leq G < 0.0688$	regular hyperbolic polygon (5 vertices)
5	$0.0688 \leq G$	circle

Table D.1.   Formulas for A_n, L_{ns} and L_{nw} for different cross sections.

Irregular Hyperbolic Triangle	Regular Hyperbolic Polygon
$A_n = \sqrt{R_1 R_2 R_3 (R_1 + R_2 + R_3)}$	$A_n = \frac{nR^2 \sin^2 \frac{\pi}{n}}{(\cos \varphi - \sin \frac{\pi}{n})^2} \left[\cos^2 \varphi \cot \frac{\pi}{n} - \pi(\frac{1}{2} - \frac{1}{n}) + \varphi - 0.5 \sin 2\varphi \right]$
$-0.5(R_1^2 \alpha + R_2^2 \beta + R_3^2 \gamma)$	$-2nr_c R_1 \sin \varepsilon \sin \varepsilon' \cos(\varepsilon' + \varphi)$
$-\sum_{i=1}^{3} \left[2r_c R_i \sin \varepsilon^i \sin \varepsilon_i^i \cos \varepsilon_{i+1}^i \right]$	$+2nR_1^2(\varepsilon' - 0.5 \sin 2\varepsilon')$
$+\sum_{i=1}^{3} \left[R_i^2(\varepsilon_i^i - 0.5 \sin 2\varepsilon_i^i) \right]$	$+nr_c^2(\varepsilon - 0.5 \sin 2\varepsilon)$
$+\sum_{i=1}^{3} \left[R_{i+1}^2(\varepsilon_{i+1}^i - 0.5 \sin 2\varepsilon_{i+1}^i) \right]$	
$+\sum_{i=1}^{3} \left[r_c^2(\varepsilon^i - 0.5 \sin 2\varepsilon^i) \right]$,	
$(\varepsilon_4^3 = \varepsilon_1^3,\ R_4 = R_1)$	
$L_{ns} = R_1 \alpha + R_2 \beta + R_3 \gamma$	$L_{ns} = 2nR \frac{\sin \frac{\pi}{n}}{\cos \varphi - \sin \frac{\pi}{n}} [\pi(\frac{1}{2} - \frac{1}{n}) - \varphi] - 4nR_1 \varepsilon'$
$-2\sum_{i=1}^{3} \left(R_i \varepsilon_i^i + R_i \varepsilon_i^{i-1} \right),\ (\varepsilon_1^0 = \varepsilon_1^3)$	
$L_{nw} = 2r_c \sum_{i=1}^{3} \varepsilon^i$	$L_{nw} = 2nr_c \varepsilon$

Figure 1.   Shape factor range for different cross sections; for each cross section zone (y-axis),

the potential range of shape factor (G) has been shown in dashed-line.

Figure 2.   Cross sections of pore throats for a) irregular hyperbolic triangle generated by three

different tangential circles (soddy circles), b) regular hyperbolic polygon with five vertices. The

hyperbolic polygon $B_{1..5}$ has an inscribed radius R and a half corner angle φ. The edge radius

of curvature is R_1.

Figure 3.   Schematic configuration of an interface within a pore body (assumed as a prolate

spheroid) during imbibition.

Figure 4.   Schematic presentation of pore units in bright color and grains in dark color.

Figure 5.   a) Shape factor distribution for pore throats in the glass-bead medium. Pore throats classification (zone numbers are given in circles) has been made according to Table 2. b) Coordination number frequency (% number of pore bodies) of the glass beads sample.

Figure 6.   Comparison between grain size distribution resulted from the model and the experimental data.

Figure 7.   Effect of shape factor and number of vertices on corner saturation, $ş^w$, in a pore throat for a) Radius of curvature $r_c = 0.5R_{eq}$, b) Radius of curvature $r_c = 0.15R_{eq}$. All cross sections have the same cross-sectional area A_{tot}.

Figure 8.   Effect of shape factor and number of vertices on a) nonwetting-wetting corner specific interfacial area $ą^{nw}$ in a pore throat for radius of curvature $r_c = 0.5R_{eq}$, b) entry capillary pressure. Entry capillary pressures have been normalized with the entry capillary pressure for a circular tube with cross-sectional area equal to A_{tot}. All cross sections have the same cross-sectional area denoted by A_{tot}.

Figure 9.   Effect of selection of pore throat cross section on a) P^c-S^w drainage curve and b) a^{nw}-S^w drainage curve.

Figure 10.   Comparison between simulations and experiments for drainage and imbibition a) P^c-S^w curves b) a^{nw}-S^w curves.

Figure 11.   Contours of specific interfacial area and normalized differences shown in the capillary pressure-saturation plane. a) Simulated P^c-S^w-a^{nw} surface for drainage, b) Simulated P^c-S^w-a^{nw} surface for imbibition, c) Difference between (a) and (b) normalized by (a), d) Difference between simulations and experimental data normalized by experimental data. Color coding in (a) and (b) shows specific interfacial area, and in (c) and (d) it shows the normalized difference. All surfaces have been generated using natural neighboring interpolation.

Figure C.1.   A typical regular hyperbolic polygonal cross section filled with the wetting and nonwetting phases. The nonwetting-wetting interface has a radius of curvature denoted by r_c and the nonwetting area is denoted by A_n.

Figure D.1.   a) Schematic presentation of interfaces in an irregular hyperbolic triangle b) Geometry of an interface and wetting phase in vertex 1. Center of the arcs with radii R_1, R_2, and r_c are denoted by A, A', and O, respectively (see also Figure 2(a)). The angle ε_j^i is referred to the angle made by the tangent at vertex i and line connecting vertex i to the intersection of interface with edge j. The angle ε^i is referred to the angle between the tangent to the interface at its intersection with the edge i and the line connecting both ends of the interface. c) Geometry of a fluid-fluid interface and the wetting phase in the vertex of a regular hyperbolic polygon. The geometry is defined by half corner angle, φ, contact angle, θ, interface radius of curvature, r_c, inscribed radius R, and edge radius of curvature, R_1 (see also Figure 2(b))

$G = 0.079$ Circle

5-vertex
Reg.Hyp.

$0.0244 \leq G \leq 0.0688$

4-vertex
Reg.Hyp.

$0.0217 \leq G \leq 0.0625$

Reg.Hyp.
Triangle

$0.0163 \leq G \leq 0.0481$

Irreg.Hyp
Triangle

$0 < G \leq 0.0163$

Cross Section Zone

Shape Factor(G)
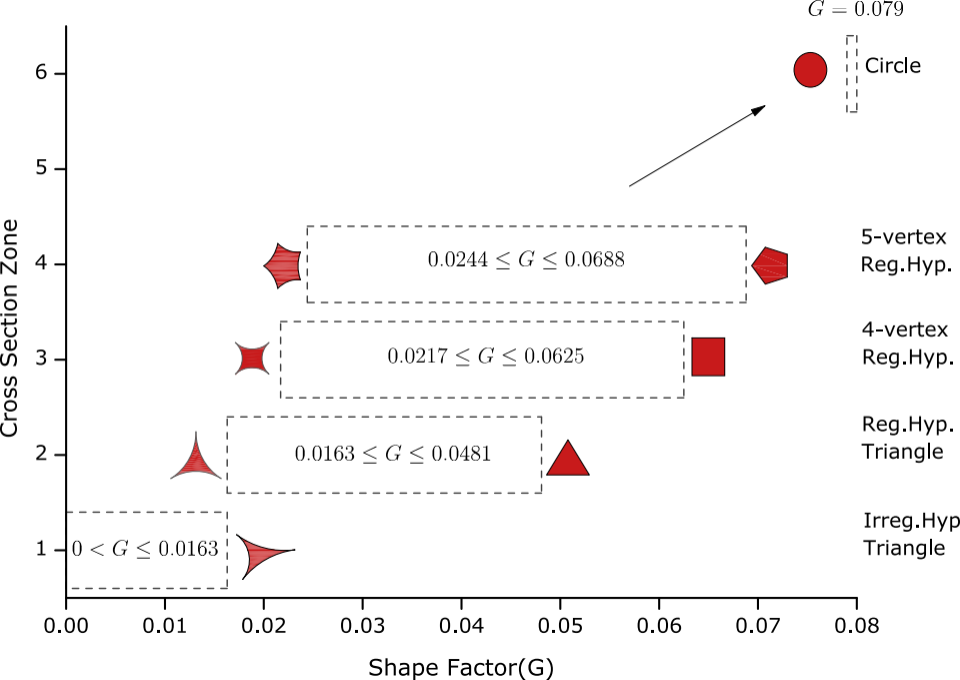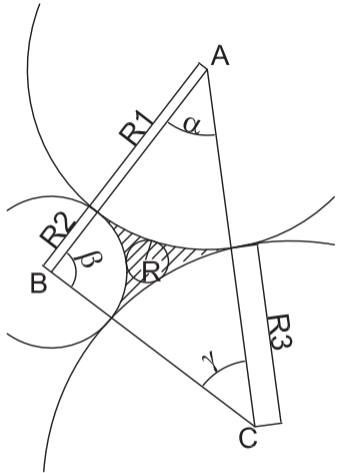
a)
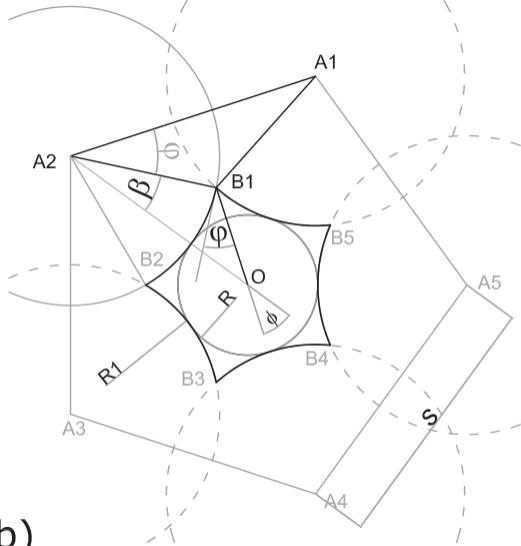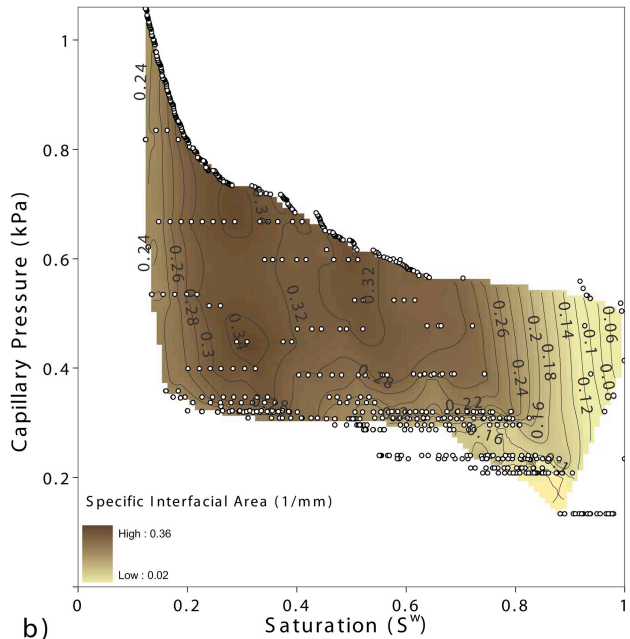
b)
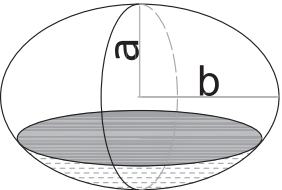
Perspective   Top View
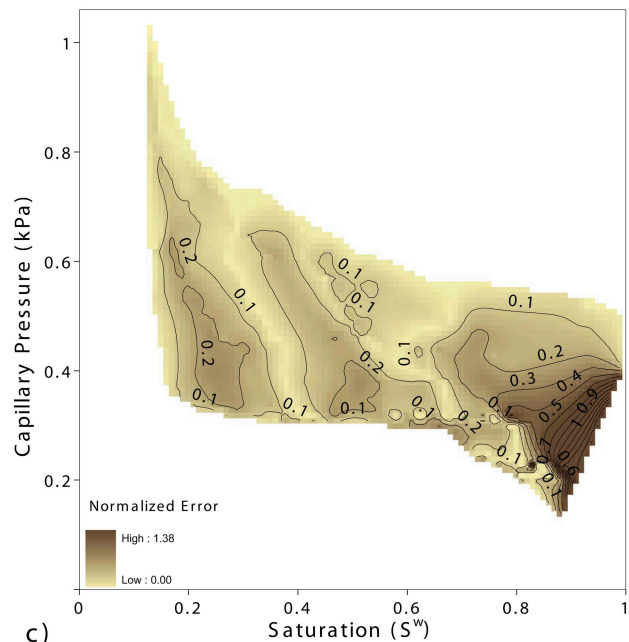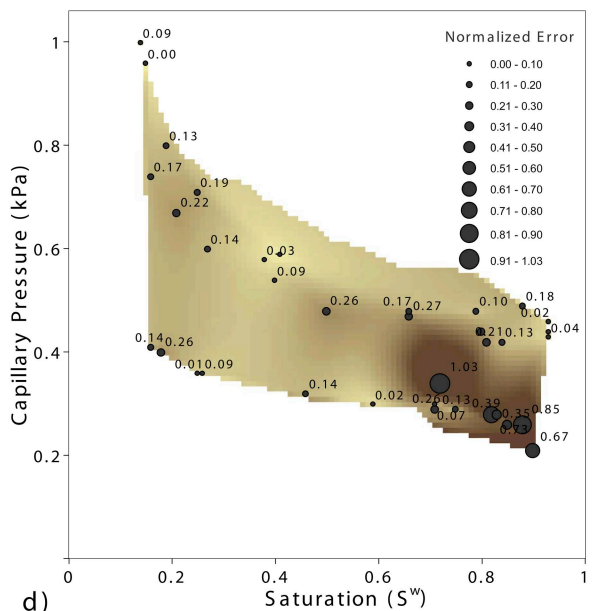
a)

b)

a)

b)

a)

b)

a)

b)

a)

b)
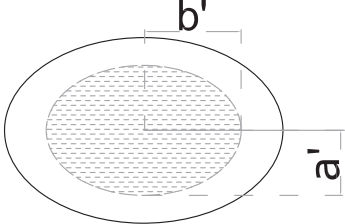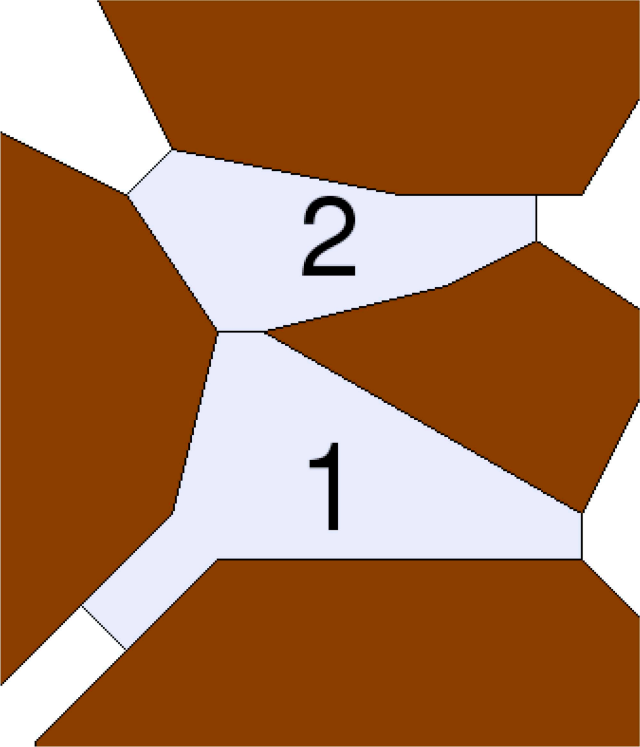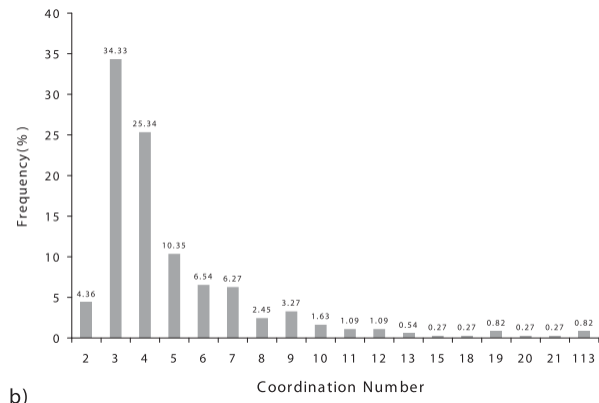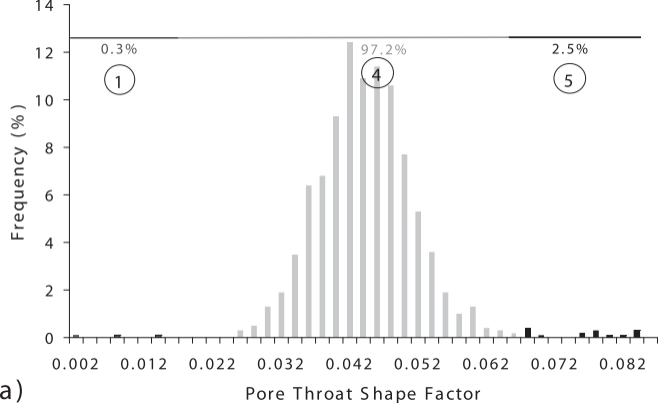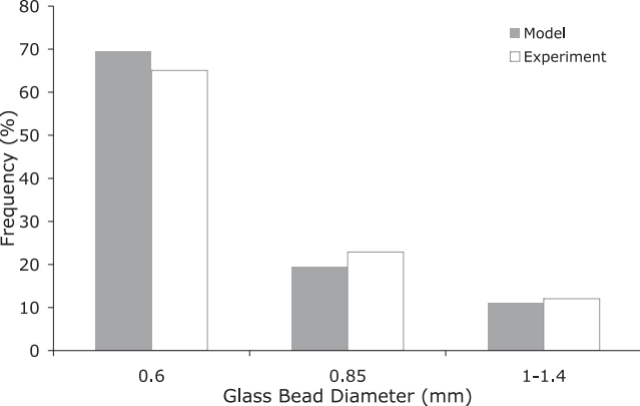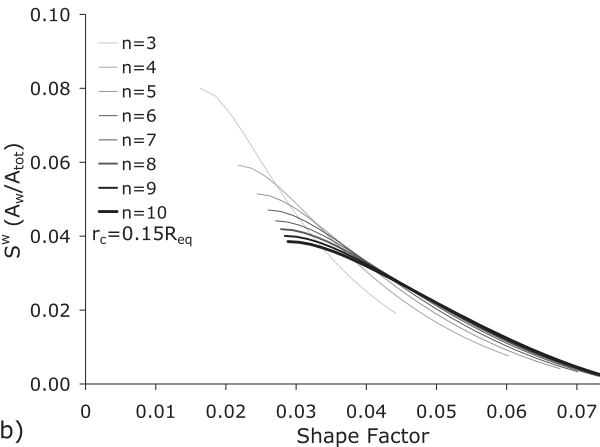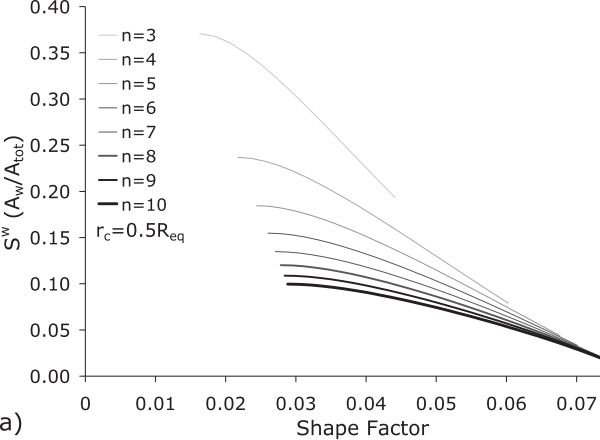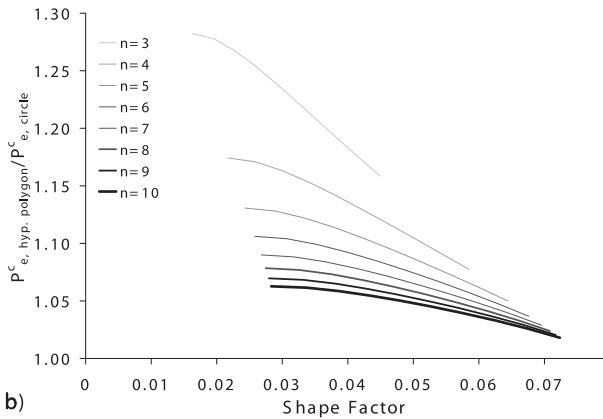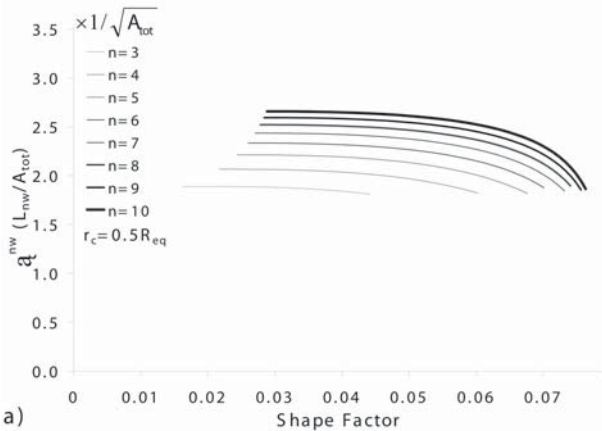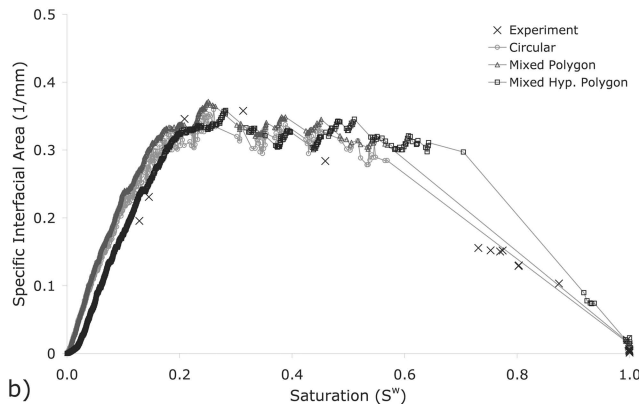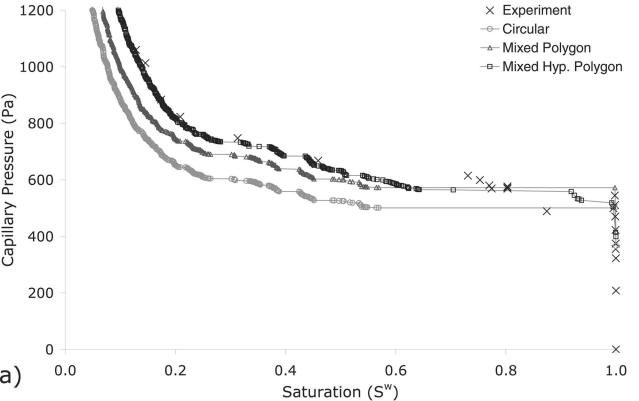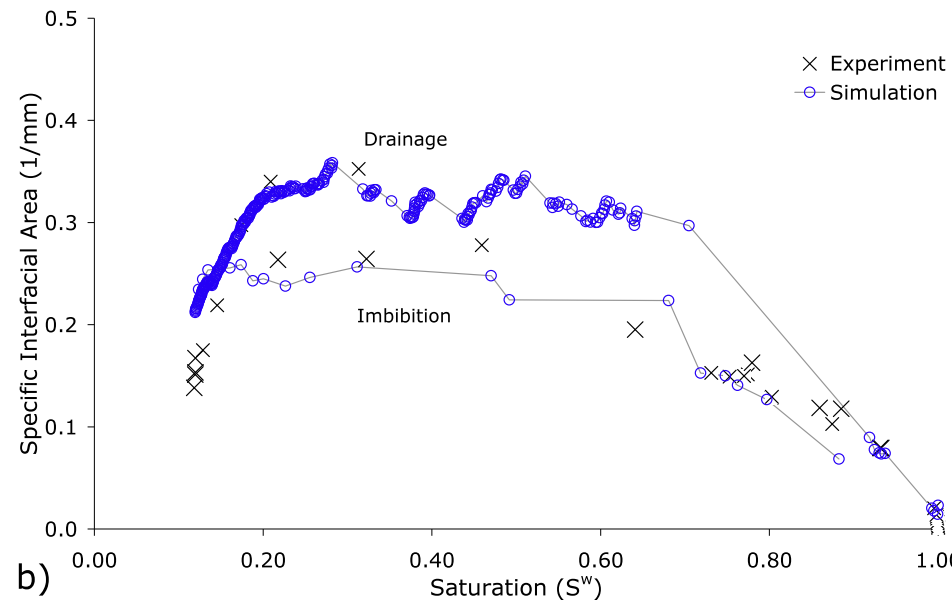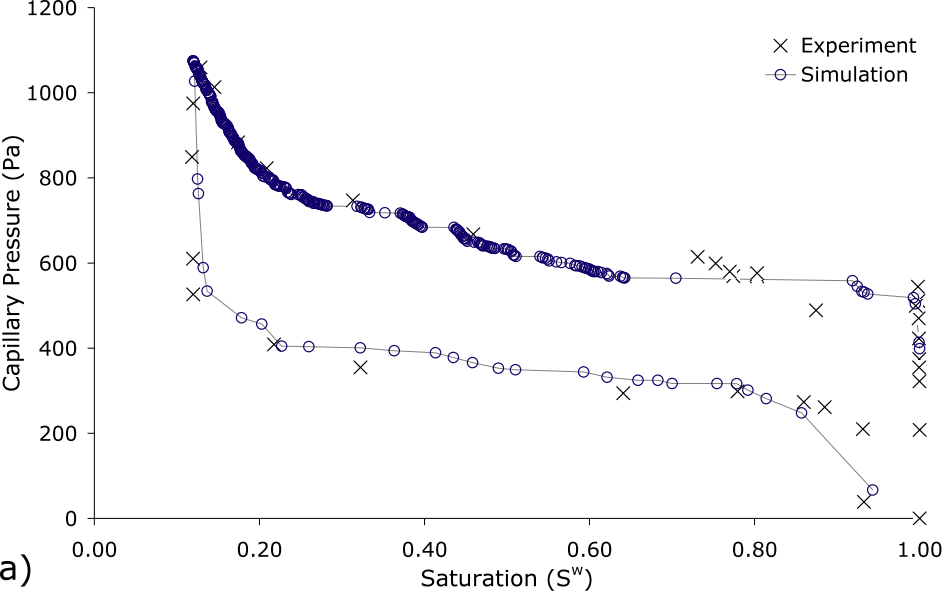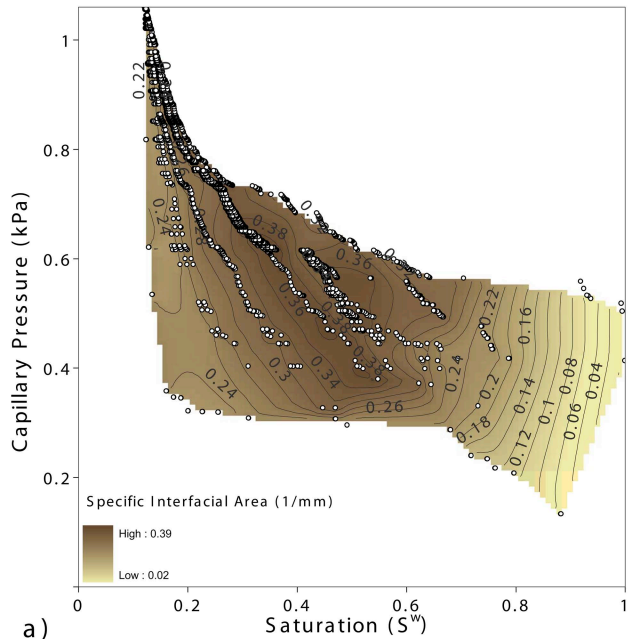
a)
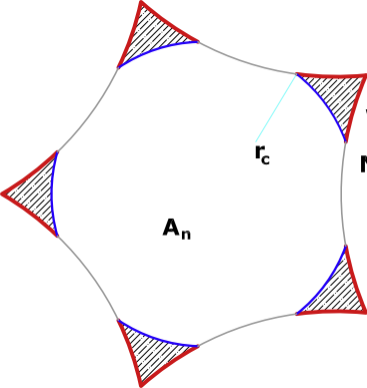
b)

c)

d)

Wetting Phase

Nonwetting Phase

L_{ns}
L_{nw}
L_{ws}

r_c

A_n

a)

b)

c)